Article

Popping and Locking: Balanced Rigidity and Porosity of Zeolitic Imidazolate Frameworks for High-Productivity Methane Purification

Tongtong Xu, Wentao Jiang, Yu Tao, Mahmoud Abdellatief, Kyle E. Cordova, and Yue-Biao Zhang*

Cite This: https://doi.org/10.1021/jacs.4c00045

Read Online

ACCESS | 📊 Metrics & More | 📰 Article Recommendations | 🆂🅸 Supporting Information

ABSTRACT: Zeolitic imidazolate frameworks (ZIFs) hold great promise in carbon capture, owing to their structural designability and functional porosity. However, intrinsic linker dynamics limit their pressure-swing adsorption application to biogas upgrading and methane purification. Recently, a functionality-locking strategy has shown feasibility in suppressing such dynamics. Still, a trade-off between structural rigidity and uptake capacity remains a key challenge for optimizing their high-pressure CO_2/CH_4 separation performance. Here, we report a sequential structural locking (SSL) strategy for enhancing the CO_2 capture capacity and CH_4 purification productivity in dynamic ZIFs (dynaZIFs). Specifically, we isolated multiple functionality-locked phases, ZIF-78-lt, -ht1, and -ht2, by activation at 50, 160, and 210 °C, respectively. We observed multiple-level locking through gas adsorption and powder X-ray diffraction. We uncovered an SSL mechanism dominated by linker−linker $\pi-\pi$ interactions that transit to C−H···O hydrogen bonds with binding energies increasing from −0.64 to −2.77 and −5.72 kcal mol^{-1}, respectively, as evidenced by single-crystal X-ray diffraction and density functional theory calculations. Among them, ZIF-78-ht1 exhibits the highest CO_2 capture capacity (up to 18.6 mmol g^{-1}) and CH_4 purification productivity (up to 7.6 mmol g^{-1}) at 298 K and 30 bar. These findings provide molecular and energetic insights into leveraging framework flexibility through the SSL mechanism to optimize porous materials' separation performance.
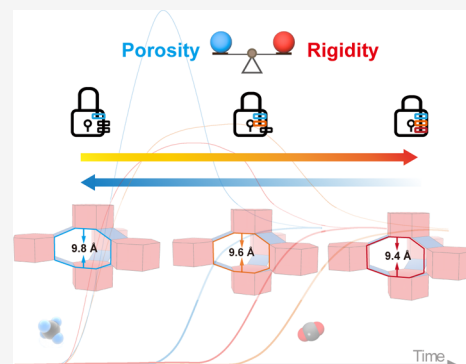
INTRODUCTION

Zeolitic imidazolate frameworks (ZIFs), metal−organic analogues of zeolites[1−6] featuring structural designability and functional porosity,[7−16] are promising porous materials for carbon capture and industrial gas separation.[17−27] However, their intrinsic structural dynamics, imposed by bendable coordination bonds and swingable linkers,[28−35] compromise their performance under practical conditions, such as high-pressure (up to 30 bar) CO_2/CH_4 gas separation for precombustion carbon capture, biogas upgrading, and liquefied natural gas (LNG) production with membrane separation or pressure-swing adsorption (PSA) techniques.[36,37] ZIFs with structural locking via external electric field or mixed metals have shown exceptional performance in membrane separation with suppressed structural dynamics,[38−42] but it remains largely untapped in PSA. Here, we report a sequential structural locking (SSL) strategy for the first time in ZIFs with balanced structural rigidity and porosity to simultaneously achieve high selectivity and high capacity in precombustion carbon capture and high-productivity methane purification with PSA techniques.
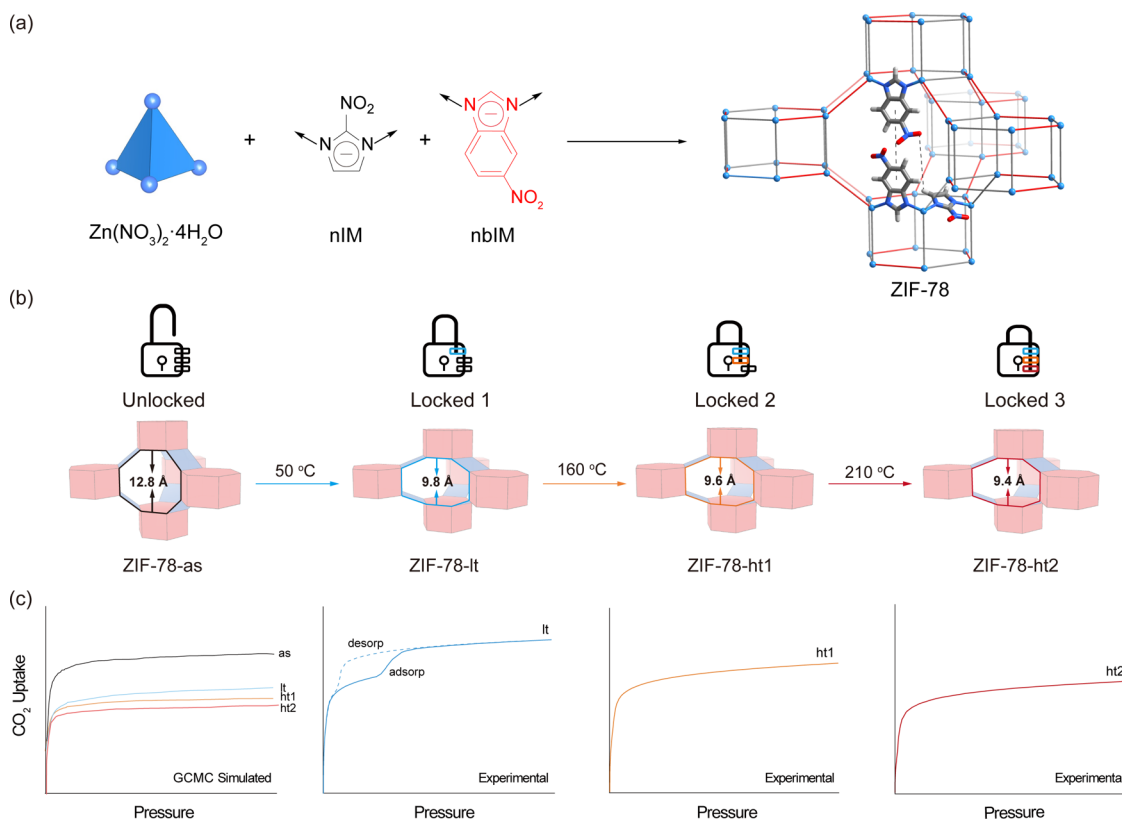
Previously, we have developed a functionality-induced structural locking method in Co(II)-based GME-ZIFs by leveraging their framework flexibility and the functionality of the imidazolate linkers (i.e., −CH$_3$, −NO$_2$) for maximizing linker−linker interactions to achieve exceptional structural rigidity and effective high-pressure CO_2/CH_4 separation.[43]

The study demonstrated that dynamic GME topology with double-6-rings (d6Rs) as rigid joints[44] and bridging 4-rings as flexible hinges provided a suitable flexible platform[45] for structural locking and emphasized the indispensable role of functionalization in maximizing linker−linker interaction and thermal activation in providing transformation energy. However, such a method imposed a trade-off between the structural rigidity and the porosity of the GME-ZIFs, decreasing their carbon capture capacity and methane purification productivity. Herein, by replacing the Co(II) metal center with Zn(II) in the GME-ZIFs, we isolated structural locking isomers via thermal-dependent activation of ZIF-78 (Scheme 1) to obtain ZIF-78-lt (lt = low temperature), -ht1 (ht = high temperature), and -ht2 at 50, 160, and 210 °C, respectively. Deliberate control of the structural locking is therefore achieved, with the distance between opposite double-6-rings (D6R) varying from 12.8 Å (unlocked) to 9.8 Å (locked 1), 9.6 Å (locked 2), and, ultimately, 9.4 Å (locked 3). Their resulting adsorption isotherms were correspondingly

Scheme 1. Design Principle for Achieving Activation-Induced Sequential Structural Locking in ZIF-78[a]

[a](a) Linking Zn(II) tetrahedral centers with 2-nitroimidazolate (nIM) and 5-nitrobenzimidazolates (nbIM) produced ZIF-78, with double-6-rings (D6R) as rigid joints and bridging 4-rings as flexible hinges to form a dynamic topology; (b) evolution of ZIF-78 from unlocked ZIF-78-as to fully locked ZIF-78-ht2 through three levels of structural locking, induced by thermal activation at 50, 160, and 210 °C, respectively; (c) relationship between experimental and simulated CO_2 adsorption isotherms for three structural locking phases in ZIF-78. With the sequential increase in structural locking degree, the CO_2 saturated adsorption capacity decreased gradually in both experiment and simulation, accompanied by increased structural rigidity.

fine-tuned from stepwise adsorption and hysteric desorption to steep adsorption with varied uptake capacities. Single-crystal X-ray diffraction (SCXRD) structures revealed an SSL mechanism arising from the $\pi-\pi$ interactions between 5-nitro-benzimidazolates (nbIM) that transit to the C−H···O hydrogen bonds with another 2-nitroimindazolate (nIM). The Hirshfeld partition of molecular density (IGMH) analyses and density functional theory (DFT) calculations reveal that the binding energy strengthened from −0.64 to −2.77 and −5.72 kcal mol^{-1}. With the balanced rigidity and porosity, a medium-level locked structure with suitable pore size and high-pressure CO_2 uptake capacity was obtained and demonstrated to exhibit superior CO_2/CH_4 separation performance with CH_4 purification productivity as high as 7.6 mmol g^{-1} at 298 K and 30 bar. The results reported herein manifest the power of the SSL strategy to enhance the utility of ZIF materials and enable their industrial applications in adsorptive gas separation processes.

■ EXPERIMENTAL SECTION

Preparation and Characterization of Structural Locking Isomers. As-synthesized ZIF-78 (ZIF-78-as) was prepared through a protocol modified from the literature,[19] in which a solvothermal reaction of Zn(NO$_3$)$_2$·4H$_2$O with nIM and nbIM in N,N-dimethylformamide (DMF) was carried out at 85 °C for 6 days (Section S1 in the Supporting Information, SI). The resulting solid was isolated and washed with fresh DMF to yield ZIF-78-as. The

crystal morphology of ZIF-78-as was examined by a scanning electron microscope (Phenom-World BV, Prox; Figure S1 in SI). ZIF-78-as was fully exchanged with absolute ethanol (EtOH) for 6 days. Three structural locking isomers, ZIF-78-lt, -ht1, and -ht2, were obtained by thermal-dependent activation heating at 50, 160, and 210 °C under a vacuum overnight.

All of the obtained activated samples possess the same chemical formula of Zn(nIM)(nbIM). The full removal of guest molecules for these isomers was confirmed by thermogravimetric analysis (TGA; Figure S2 in SI), Fourier-transform infrared spectroscopy (FTIR; Figure S3 in SI), and digested-solution ^{1}H nuclear magnetic resonance spectroscopy (NMR; Figures S4−S6 in SI). TGA measurements were performed on a TGA instrument (PerkinElmer, TGA 4000) with a heating rate of 5 °C min^{-1} from ambient temperature to 700 °C under N$_2$ flow, demonstrating high thermal stability (300 °C). Solid-state ^{1}H nuclear magnetic resonance (SSNMR) spectroscopy was performed with magic angle spinning (MAS) techniques on a Bruker AVANCE III HD 400 MHz wide-bore solid-state NMR spectrometer at a magnetic field of 9.4 T equipped with a standard Bruker MAS probe with a 3.2 mm (o.d.) zirconia rotor. The ^{1}H chemical shifts were calibrated by the hydrogen of the adamantane reference sample assigned to 1.91 ppm (Figure S7 in SI). Differential scanning calorimeter (DSC) measurements were performed by heating and cooling the samples on a TA DSC Q2000 instrument, with a heating rate of 40 K min^{-1} under the N$_2$ atmosphere (Figure S50 in SI).

X-ray Diffraction. Single-crystal X-ray diffraction (SCXRD) data of the as-synthesized and activated ZIF-78 were collected by using synchrotron X-ray radiation (λ = 0.6705 or 0.6887 Å) at beamline
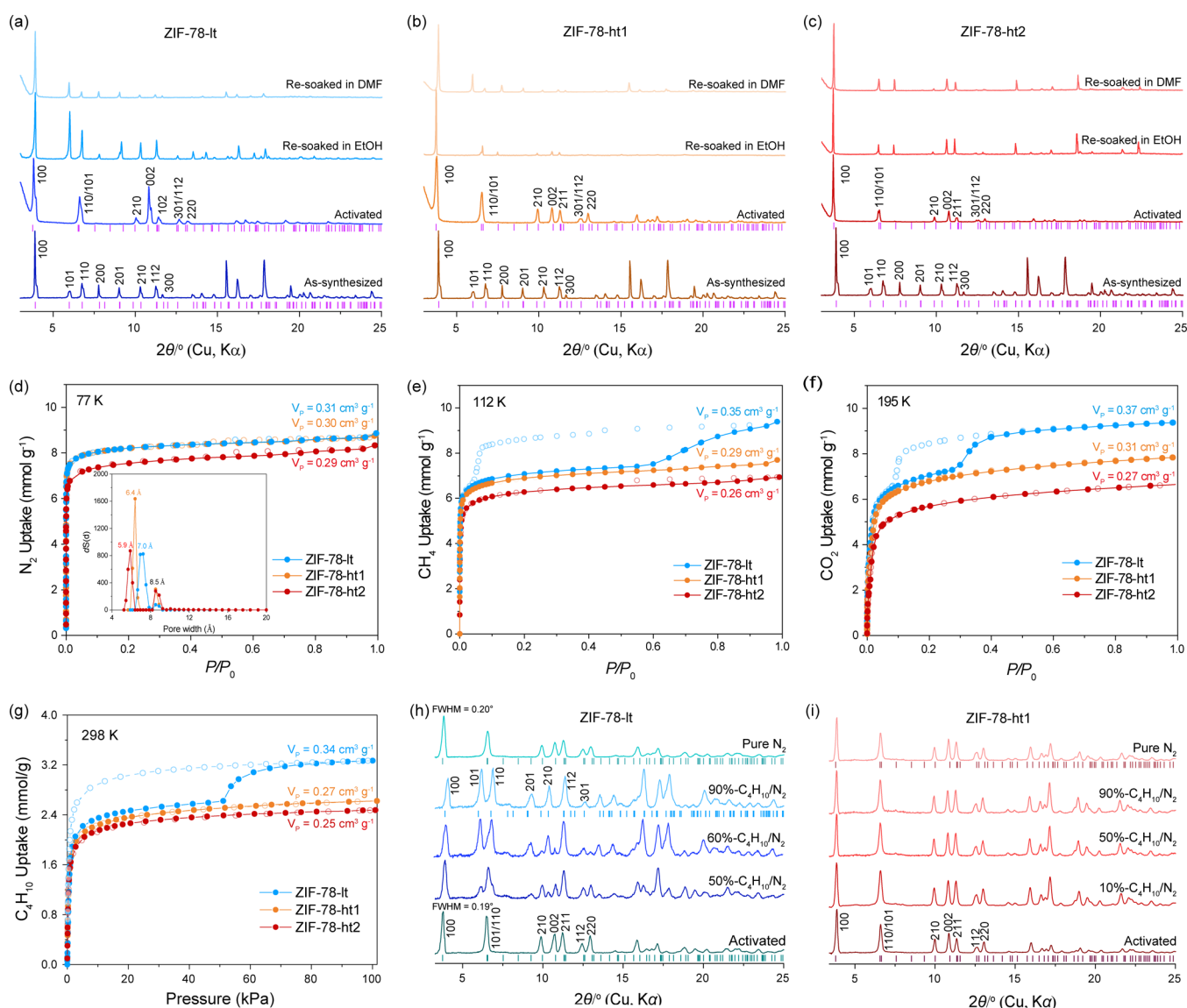
Figure 1. Revealing the dynamic behavior of different activated phases of ZIF-78 by comparing as-synthesized/activated PXRD patterns, gas/vapor adsorption isotherms, and the as-synthesized sample immersed in DMF. Indexed PXRD patterns of (a) ZIF-78-lt showed reversible unit cell changes in both EtOH and DMF; (b) ZIF-78-ht1 displayed irreversible unit cell changes in EtOH with lower polarity and reversible changes in DMF with higher polarity; (c) ZIF-78-ht2 exhibited irreversible unit cell changes in both EtOH and DMF. Gas adsorption isotherms for ZIF-78-lt ZIF-78-ht1, and ZIF-78-ht2 with sequential structural locking of (d) N_2 at 77 K, (e) CH_4 at 112 K, (f) CO_2 at 195 K, and (g) C_4H_{10} at 298 K. The data demonstrated that the structures of ZIF-78-ht1 and ZIF-78-ht2 were rigid, while ZIF-78-lt was flexible. *In situ* PXRD patterns under various C_4H_{10}/N_2 gas flows at 298 K for (h) ZIF-78-lt and (i) ZIF-78-ht1 demonstrate their flexible or rigid structures, respectively, upon guest inclusion and removal.

BL17B of the Shanghai Synchrotron Radiation Facility (SSRF). The activated samples were sealed in 0.3 mm inner diameter (I.D.) borosilicate-glass capillaries under an argon atmosphere in a glovebox equipped with an optical microscope (Section S2 in SI).

Powder X-ray diffraction (PXRD) patterns of as-synthesized, activated, and resolved samples were recorded on a Bruker D8 Advance diffractometer with Cu-Kα radiation (λ = 1.5418 Å), which were collected in the 2θ range of 3−40° with a step size of 0.02°. The PXRD patterns of ZIF-78-lt, -ht1, and -ht2 used for Pawley refinement were collected at beamline BL14B1 of SSRF using synchrotron radiation with a wavelength of 0.6895 Å. The samples were sealed in 0.8 mm (I.D.) borosilicate-glass capillaries. Dynamic gas adsorption *in situ* PXRD measurements were performed on a Bruker D8 Advance diffractometer equipped with an *in situ* Anton Paar XRK 900 chamber under the adsorptive flow of C_4H_{10} carried by dry N_2 with concentration varied by a customized gas mixer (Section S3 in SI). The PXRD patterns were collected continuously under a constant

concentration until equilibrium was reached to track the kinetics of structural transformation before switching to another concentration.

Gas Adsorption. Ultrahigh-grade gases (99.999%), such as He, N_2, CO_2, and CH_4, were used throughout the experiments. Low-pressure gas/vapor adsorption isotherms were measured volumetrically by using a Quantachrome iQ (CO_2 and CH_4) or Microtac BELsorp Max2 (N_2, C_4H_{10}, and H_2O) sorption analyzer. The heat of adsorption of C_4H_{10} at 298 K was measured using a Microtac BELsorp Max2 sorption analyzer coupled to differential scanning calorimetry (SenSys EVO, Setaram). High-pressure adsorption isotherms (0−30 bar) were measured on a Quantachrome iSorb HP1 instrument. High-pressure dynamic adsorption breakthrough curves were evaluated by using a Hiden ABR automated breakthrough analyzer (Sections S4−S8 in SI).

Computational Analyses and Molecular Simulation. For qualitative analysis of linker−linker interactions, electrostatic potential (ESP)-colored van der Waals surface maps of the representative

C

segments of ZIFs were calculated based on the effective algorithm implemented by Multiwfn.[46,47] The input files containing wave function information were generated by Gaussian 09 W in the ground-state DFT method at B3LYP/6-311G** level. The segments that illustrate the distinct interactions were clipped from the single-crystal X-ray structures of ZIF-78-as, -lt, ht1, and ht2. Moreover, the quantum theory of atoms in the molecules (QTAIM) method and the electron localization function (ELF) two-dimensional (2D) maps of these segments were generated by Multiwfn for further comprehensive comparison (Section S9 in SI).

For quantitative analyses of linker−linker interactions, analyses of the independent gradient model based on Hirshfeld partition of molecular density (IGMH)[48] for the periodic crystal structures of ZIFs were conducted by Multiwfn. For these ZIFs with periodic structure, CP2K software was used for generating the wave functions by DFT calculation using PBE-D3(BJ) exchange−correlation function with DZVP-MOLOPT-SR-GTH level (Section S9 in SI). The interlinker binding energies of ZIF-78-lt, ht1, and ht2 were further evaluated by the QTAIM method (Section S9 in SI).[49]

Grand canonical Monte Carlo (GCMC) simulations of CO_2 adsorption isotherms at 195 K (0−100 kPa) and 298 K (0−30 bar) were implemented in the RASPA software package.[50] The net atom charges (NACs) in the frameworks were computed using the density-derived electrostatic and chemical (DDEC) method.[51] The Lennard-Jones (LJ) parameters of the metal atoms in the framework came from the universal force field (UFF),[52] and those of the nonmetal elements came from the DREIDING force field.[53] Total number of simulation cycles was set as 200,000, with 100,000 cycles for initialization and 100,000 cycles for production, to reach the convergence, and the values were obtained by taking the average (Section 9 in SI).

■ RESULTS AND DISCUSSION

Identification of Structural Locking Isomers. The multiple levels of structural locking were observed via the reversibility of structural transformations upon activation and resolution in solvents with increasing polarities (acetone, acetonitrile, EtOH, and DMF). By comparing their PXRD patterns (Figure 1a−c), reversible structural transformation was observed for ZIF-78-lt in EtOH and DMF, while reversible structural transformation for ZIF-78-ht1 was only seen in DMF. In contrast, ZIF-78-ht2 showed irreversible structural transformation even when immersed in DMF.

Specifically, the PXRD patterns of ZIF-78-lt, -ht1, and -ht2 displayed a significant diffraction peak shift when compared to ZIF-78-as, with the 100 reflections shifting to a lower 2θ angle and the 101 and 110 reflections shifting to higher 2θ angles, thereby indicating a significant structural contraction upon guest removal (Figure S17 in SI). After being immersed in either DMF or EtOH, the PXRD patterns for the resolved ZIF-78-lt exhibited a complete recovery to that of ZIF-78-as, which suggested reversible structural flexibility for ZIF-78-lt (Figure 1a; Figure S18 in SI). Strikingly, the PXRD patterns for ZIF-78-ht1 demonstrated that its structure remained unchanged when immersed in solvents with low polarity, such as EtOH and acetone, but was recovered to ZIF-78-as in higher polar solvents, such as DMF and acetonitrile, thereby indicating it had stronger structural locking than ZIF-78-lt (Figure 1b; Figure S19 in SI). The PXRD patterns for ZIF-78-ht2 remained unchanged after immersion in any solvents, regardless of polarity, which indicated an irreversible structural transformation under the operating conditions (Figure 1c; Figure S20 in SI). The results initially demonstrated a sequential enhancement in the structural locking strength, given the varying degrees of structural flexibility observed in response to solvents with different polarities.

The flexible/rigid nature of the three structural locking isomers (Figure 1e−g) was probed during gas adsorption by adsorptives N_2 (77 K), CH_4 (112 K), CO_2 (198 K), and C_4H_{10} (298 K), respectively. All structural locking isomers exhibit type I physisorption isotherms for N_2 (77 K) with pore volumes of 0.31, 0.30, and 0.29 cm^3 g^{-1}, respectively. The pore size distributions of the three ZIFs derived from their N_2 adsorption isotherms were 7.0/8.5, 6.4/8.5, and 5.9/8.5 Å, respectively (Figure 1d), revealing multiple levels of structural locking.

Significant two-step adsorption isotherms followed by non-negligible hysteresis loops were observed in ZIF-79-lt for CH_4 (112 K), CO_2 (195 K), and C_4H_{10} (298 K), suggesting its flexing nature during gas adsorption. Dynamic gas adsorption *in situ* PXRD patterns of ZIF-78-lt (Figure 1h; Figure S21 in SI) demonstrated its dynamic responses under various C_4H_{10}/N_2 concentrations at 298 K. Significant PXRD pattern changes started under 50% C_4H_{10}/N_2 concentration, corresponding to the second uptake at ∼50 kPa in the static gas adsorption (Figure 1g, Figure S22 in SI). Specifically, the 100 reflections at 3.98° shifted to a higher 2θ angle, indicating a decrease in the a-axis. The 110/101 reflections at 6.76° split into two diffraction peaks at 6.38 (101) and 6.91° (110), suggesting an increase in the c-axis. Lower diffraction intensity and broad peaks were generally observed upon gas adsorption for ZIF-78-lt, which can be attributed to the dynamic feature of the framework and the influence of adsorbates. High intensity and sharp peaks of ZIF-78-lt observed upon desorption by purging dry N_2 at room temperature demonstrated the reversibility of the dynamic responses and the retention of high crystallinity, as evidenced by the similar full width at half-maximum (fwhm) before and after C_4H_{10} adsorption (0.189 and 0.202, respectively). At the point of structural transformation, the C_4H_{10} gas adsorption *in situ* microcalorimetry of ZIF-78-lt at 298 K showed an anomalous drop of exothermic intensity (Figure S49 in SI), showing its potential for thermal management of adsorption heat by utilizing the endothermic effect of structural transition. All of these results support that the GME-ZIF can be a flexible framework to show reversible dynamic responses to gas molecules.

With structural locking, both ZIF-78-ht1 and -ht2 exhibited one-step knee-shaped adsorption isotherms for all of the CH_4 (112 K), CO_2 (195 K), and C_4H_{10} (298 K), indicating their rigidity during gas adsorption. More interestingly, ZIF-78-ht1 exhibits higher gas uptakes than ZIF-78-ht2, illustrating a delicate balance of rigidity and porosity. Dynamic gas adsorption *in situ* PXRD patterns for ZIF-78-ht1 (Figure 1i; Figure S23 and SI) showed that the diffraction peak positions remained unchanged with variations to only the intensities of those diffraction peaks due to the gas adsorption under various C_4H_{10}/N_2 concentrations.

Molecular and Energetic Insights into the Structural Locking Isomers. Temperature-dependent *in situ* PXRD patterns of ZIF-78-as under N_2 showed that the structural transformation to ZIF-78-lt began at 75 °C (Figure S24 in SI). Furthermore, an irreversible endothermic effect was observed in the DSC measurements of ZIF-78-lt at 146 °C, indicating that the transition to the ZIF-78-ht1 phase is a non-spontaneous process (Figure S50 in the SI). No negligible endothermic peak can be observed between the transition of ZIF-78-ht1 and -ht2, revealing that the ZIF-78-ht1 is a metastable phase and -ht2 is a global stable phase. Similar water adsorption isotherms were observed for all three phases
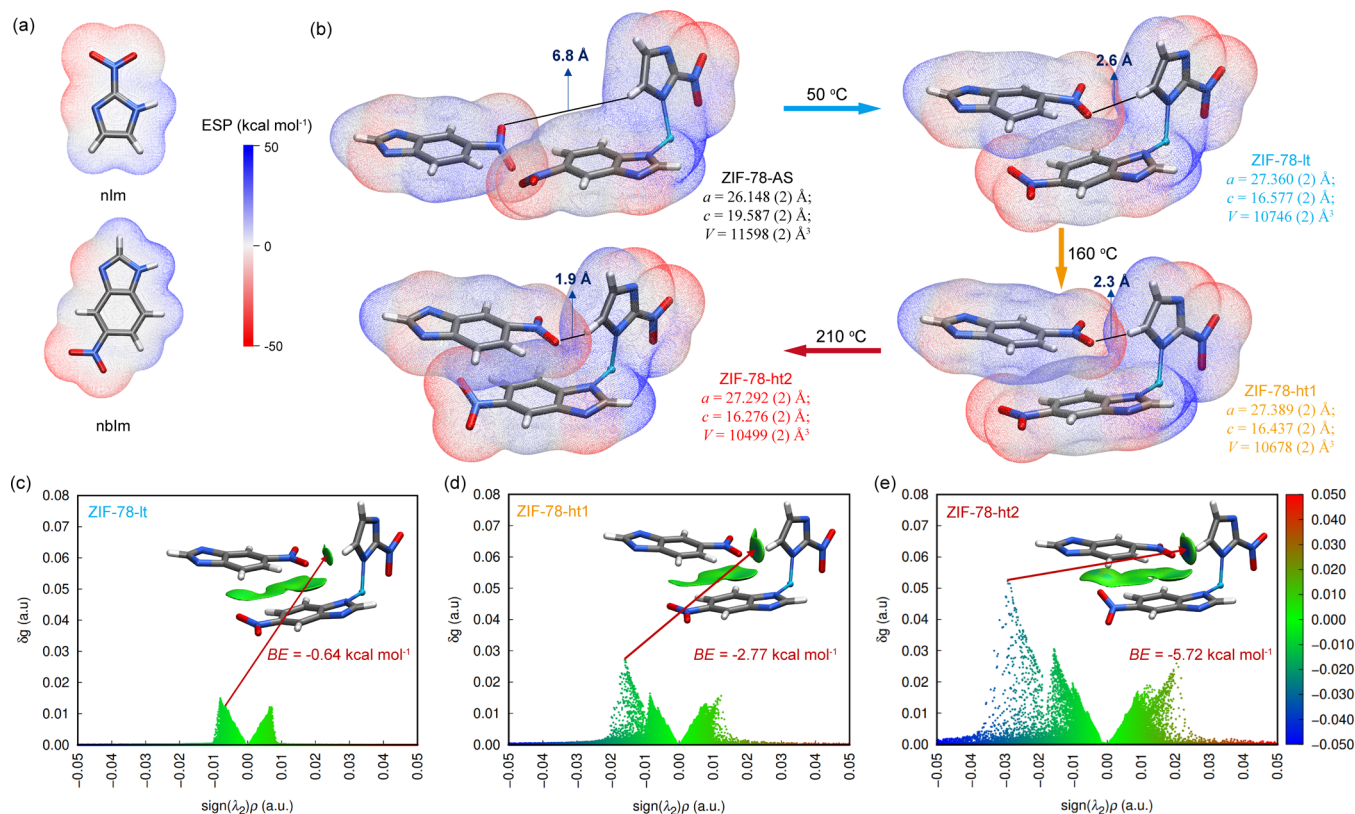
Figure 2. Structural transformations of dynamic ZIF-78 upon guest removal were characterized by SCXRD analyses. Illustration of the dynamic locking mechanism observed for the frameworks by linker−linker interactions in ESP-colored van der Waals surface maps of (a) imidazole organic linkers used in this work; (b) truncated segments of ZIF-78-as and three sequential structural locking phases; independent gradient model based on IGMH analyses for (c) ZIF-78-lt, (d) ZIF-78-ht1, and (e) ZIF-78-ht2. The ESP maps are colored from −50 to 50 kcal mol^{-1} on the system's van der Waals surface ($\rho = 0.001$ a.u.). In IGMH scatter graphs, ρ is the electron density that is positively correlated with the interaction strength (λ_2), which is the sign of the second largest eigenvalue of the Hessian matrix whose value can distinguish whether the interaction is attractive (negative) or repulsive (positive). δg is the difference between g^{IGM}, the IGM-defined density gradient, and g, the density gradient, which positively correlates with the intermolecular interaction strength. BE is the binding energy of the intermolecular hydrogen bonds. The isosurface of δg was plotted with an isovalue of 0.0045 a.u., and the color range is from −0.05 to 0.05 a.u.

of ZIF-78-lt, -ht1, and -ht2 (Figure S26 in SI), showing the hydrophilicity of the functional groups independent of the activation temperatures.

The single-crystal X-ray structures of ZIF-78-as, -lt, -ht1, and -ht2 provided a fundamental understanding of the dynamic structural transformation at the atomic level (Figure 2). All phases were isostructural and crystallized in space group $P6_3/mmc$ (No. 194). Each tetrahedral Zn(II) center is connected to two nIMs and two nbIMs that were interconnected to form a three-dimensional framework with GME net, which is isoreticular to the Co(II)-based structures.[43] To handle the substantial disorder of nbIM, the activated structures were refined in lower symmetry space group $P6_3$ (No. 173). For ZIF-78-as, -lt, -ht1, and -ht2, the Zn−N bond lengths decreased from 2.01 to 1.95, 1.93, and 1.90 Å, respectively, which was consistent with the tendency observed in ZIF-78-Co, where the bond lengths for as-synthesized and activated phases were 2.01 and 1.88 Å, respectively. Accordingly, the N−Zn−N bond angles between nIM, zinc, and nbIM increased from 104.9 to 107.0, 111.4, and 112.3°, respectively, while in ZIF-78-Co, the corresponding angles increase was from 99.5 to 111.7°. The variation may be ascribed to the disappearance of interactions between solvent and linker after activation, causing a charge rearrangement and an increase in linker electro-

negativity, in accordance with Gutmann's bond length variation rules.[54]

Compared to ZIF-78-as, the length of the a-axis for ZIF-78-lt, ht1, and -ht2 increased from 26.148 to 27.365, 27.389, and 27.375 Å, respectively, whereas the length of the c-axis was reduced from 19.587 to 16.579, 16.437, and 16.146 Å, respectively. The evolution in unit cell parameters demonstrated a significant reduction in cell volume, with values of 7.29, 7.93, and 9.66% for ZIF-78-lt, -ht1, and -ht2, respectively, which indicated a sequential structural contraction upon thermal activation. The theoretical pore volume and pore size calculated by using CO_2 as a probe also proved the sequential contraction, in which the pore volumes of ZIF-78-as, -lt, -ht1, and -ht2 decreased from 0.34 to 0.26, 0.25, and 0.23 cm^3 g^{-1}, respectively, and the pore size decreased from 4.66 to 3.48, 2.97, and 2.76 Å, respectively. The results were consistent with the pore volumes calculated from GCMC simulations, which were lower than the experimental results due to the completely rigid structures treated in the simulation. In addition, the flexibility of ZIF-78-lt in reverting to ZIF-78-as during the adsorption process could also be proven from the simulation (Scheme 1c, Figures S25 in SI).

ESP-colored van der Waals surface maps were used to qualitatively understand the distribution of electrostatic potential around the linkers and provide insights into the
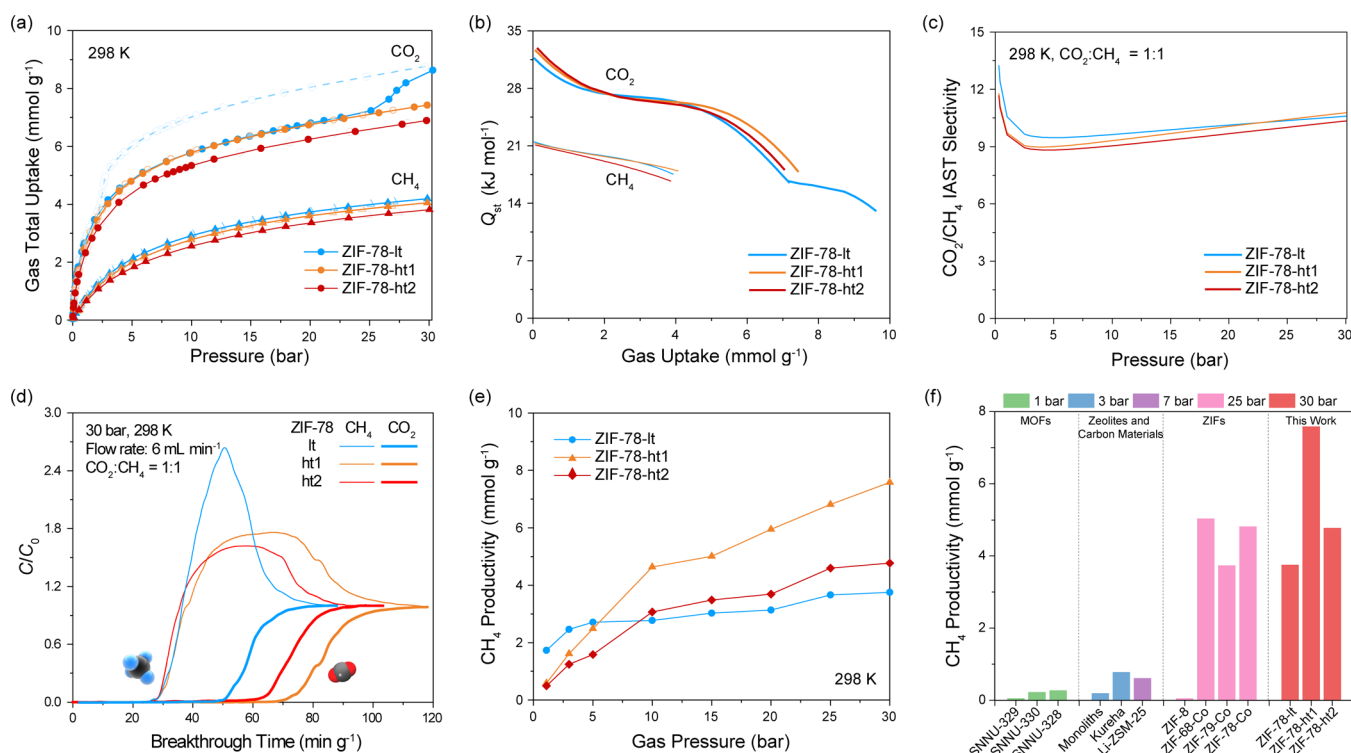
Figure 3. Evaluation of the CO_2/CH_4 adsorptive separation performance via high-pressure gas uptake isotherms and dynamic breakthrough measurements. (a) High-pressure total CO_2 and CH_4 uptake isotherms at 298 K for ZIF-78-lt (blue), -ht1 (orange), and -ht2 (red). (b) Heats of CH_4 and CO_2 adsorption were derived from their high-pressure adsorption isotherms for four temperatures using virial model fitting. (c) Pressure-dependent CO_2/CH_4 selectivity based on the IAST model. (d) Dynamic adsorption breakthrough curves for ZIF-78 at 298 K and 30 bar with a 1:1 (v/v) ratio of CH_4 and CO_2 and a 3 mL min^{-1} flow rate. (e) The purification productivity of CH_4 calculated by integrating the CO_2/CH_4 breakthrough curve (CO_2/CH_4 = 50:50) at 298 K, with CH_4 purity of 99%. (f) Comparison of CH_4 purification productivity calculated from CO_2/CH_4 breakthrough curve (CO_2/CH_4 = 50:50) at 298 K for ZIFs in this work with our previous work[43] as well as MOFs, zeolites, and carbon materials[57−60] previously reported. The blue, orange, and red pentagrams represented ZIF-78-lt, ZIF-78-ht1, and ZIF-78-ht2, respectively; the orange, red, and blue hollow circles represented ZIF-68-Co, ZIF-78-Co, and ZIF-79-Co, respectively; the green triangles represent MOFs, and the gray diamonds represent zeolites (solid diamonds indicate the breakthrough test conducted at 298 K, while hollow diamonds represent test at 303 K).

positive and negative charge density of individual atoms (Figure 2a,b). Accordingly, DFT calculations were performed to analyze the linker−linker interactions of ZIF-78-as and the three activated phases. The analysis of linkers demonstrated that both hydrogen atoms on nIM and benzene rings were electropositive, while the nitro group was electronegative, implying that potential attractive interaction may occur between them (Figure 2a). Compared to ZIF-78-as without interaction between nIM and adjacent nbIM, the obvious attraction was observed in ZIF-78-lt, -ht1, and -ht2, which may be classified as hydrogen bond due to the electronegative oxygen and electropositive hydrogen.[55,56] This interaction gradually increased as the distance between the nitro group and the hydrogen atom decreased (from 2.6 to 2.3 and 1.9 Å), as inferred from the enhanced overlap of the electron cloud density. Solid-state ^{1}H NMR spectroscopy for ZIF-78-lt, -ht1, and -ht2 as well as the two imidazole linkers exhibited downfield shift upon hydrogen bond formation. Although solid-state ^{1}H NMR spectra were generally broad due to the resolution limitation, significant downfield shifts were observed by the elimination of 0.39 and 2.69 ppm and the shoulder of 7.86 ppm chemical shifts for ZIF-78-ht2 (Figure S7 in the SI).

The interaction between two nbIMs in ZIF-78-as was mainly a repulsive interaction contributed by nitro groups in which the framework was stabilized through interactions with solvent molecules. For ZIF-78-lt, -ht1, and -ht2, a significant attraction

was observed between the nitro group and benzene ring with conjugation, which may be classified as an π−π interaction. Similarly, this attraction also strengthened, as evidenced by the expanded interaction area (Figure 2b). Two attractive interactions with different strengths synergistically achieved sequential structural locking in ZIF-78.

To quantitatively analyze and visualize the interactions between linkers, IGMH analysis was conducted (Figure 2c−e). The weak interactions were illustrated by isosurfaces colored according to the electron density values. Based on the same isovalue, isosurfaces with larger areas and bluer colors represented larger interaction regions and stronger strengths. The results showed that π−π interaction between two nbIMs was enhanced with the increasing locking degree, which was consistent with ESP results. To evaluate hydrogen bonds, binding energy (BE) was fitted by the electron density at the bond critical point (BCP) from QTAIM analyses with values of −0.64, −2.77, and −5.72 kcal mol^{-1} for ZIF-78-lt, -ht1, and -ht2, respectively. The values represented weak electrostatic attraction between nIM and an adjacent nitro group of nbIM in ZIF-78-lt, while weak and strong hydrogen bond interaction in ZIF-78-ht1 and -ht2, respectively. QTAIM electron density topology and ELF density analysis as well as atom charge comparison using different calculation methods were conducted to further clarify the nature of the hydrogen bond (Table S18, Figure S69 in SI). The results highlighted the

synergistic importance of linker—linker interactions in structural locking.

High-Productivity CH$_4$ Purification via Pressure-Swing Adsorption. The thermodynamic behavior of CO$_2$/CH$_4$ separation for ZIF-78-lt, -ht1, and -ht2 was evaluated from high-pressure (0–30 bar) CO$_2$ and CH$_4$ static adsorption isotherms (Figures S31–S36 in SI). As shown in Figure 3a, all ZIFs exhibited a higher adsorption affinity and uptake capacity for CO$_2$ over CH$_4$. The CO$_2$ uptakes for ZIF-78-lt, -ht1, and -ht2 at 298 K and 30 bar were 8.8, 7.4, and 7.0 mmol g^{-1}, respectively, 2- to 3-fold higher than the CH$_4$ uptake.

Consequentially, the CH$_4$ and CO$_2$ heats of adsorption (Q_{st}), as derived from high-pressure adsorption isotherms and fitted with the virial model, suggested stronger interactions between CO$_2$ and each of the frameworks (Figure 3b). When 1 mmol g^{-1} of gas was adsorbed, CO$_2$ heats of adsorption for ZIF-78-lt, -ht1, and -ht2 were 28.5, 29.2, and 29.6 kJ mol^{-1}, respectively, while CH$_4$ heats of adsorption were 20.4, 20.3, and 20.1 kJ mol^{-1}, respectively, which was consistent with the simulated CO$_2$ heats of adsorption derived from GCMC simulation (Figure S48 in SI).

Using CO$_2$ and CH$_4$ adsorption data, ideal adsorbed solution theory (IAST) was applied to estimate the CO$_2$/CH$_4$ selectivity of the frameworks (Figure 3c). Specifically, for an equimolar mixture of CO$_2$ and CH$_4$ at 298 K and 30 bar, the adsorption selectivities of ZIF-78-lt, -ht1, and -ht2 were 10.6, 10.8, and 10.3, respectively, which were comparable with several state-of-the-art MOFs for CO$_2$/CH$_4$ separation (Table S15 in SI). It is worth noting that due to its higher adsorption capacity for CO$_2$, ZIF-78-lt exhibited a slightly higher overall selectivity than ZIF-78-ht1 and -ht2. The influence of sequential structural locking on the kinetic separation performance was then demonstrated via dynamic breakthrough experiments of CO$_2$/CH$_4$. As shown in Figure 3d, an efficient separation for a 1:1 ratio CO$_2$/CH$_4$ mixture was achieved by ZIF-78-lt, -ht1, and -ht2. As expected, CH$_4$ was the first gas to elute through the adsorption bed with a high-purity grade of 99%, and the corresponding productivities of CH$_4$ at 30 bar were 3.8, 7.6, and 4.8 mmol g^{-1} for ZIF-78-lt, -ht1, and -ht2, respectively. At the same time, CO$_2$ was retained for a significant amount of time, with the working capacity calculated to be 13.1, 18.6, and 14.9 mmol g^{-1}, respectively. Strikingly, ZIF-78-ht1, with a balanced rigidity and porosity, exhibited the best separation performance among these ZIFs, as highlighted by the highest CO$_2$ working capacity and CH$_4$ purification productivity (Figure 3e; Figures S66–S67 in SI).

Strikenly, ZIF-78-ht1 represents the highest CH$_4$ productivity among the ZIFs reported here, those evaluated in our previous study[43] as well as other MOFs, zeolites, and activated carbon in the literature (Figure 3f).[57−60] The multiple stable conformations achieved in ZIF-78-Zn may be attributed to the d^{10} configuration of Zn(II) tetrahedral center with zero crystal field stabilization energy (CFSE),[61] resulting in lower energy barriers for conformational transitions and easier attainment of multiple local energy minima. In contrast, isoreticular ZIF-78-Co with d^7 Co(II) tetrahedral centers had a higher CFSE equal to $-1.2\Delta_t$ (Δ_t is the tetrahedral crystal field splitting energy), making it more determinative for structural transformation. Indeed, the dihedral angle deviations of tetrahedra in ZIF-78-Zn and ZIF-78-Co were found to be 0.06 and 0.47%, respectively, suggesting that coordination geometry distortion occurred in ZIF-78-Co might trap the framework in a deeper energy minimal.[62,63]

Considering industrial settings, low-energy consumption and time efficiency throughout the regeneration and recycling processes are important features.[64−66] For ZIF-78, with its sequential structural locking phases, regeneration was fully realized under mild conditions by simply purging the ZIF-containing bed with Ar at ambient temperature. With a rigid structure induced by structural locking, ZIF-78-ht2 exhibited great durability under high pressure, as proved by high-pressure CO$_2$ adsorption and dynamic breakthrough measurements at 30 bar and 298 K (Figures S37, S65 in SI).

■ CONCLUSIONS

By controlling linker dynamics in ZIFs through functionality-induced locking, we uncover a sequential structural locking mechanism for balancing the structural rigidity and porosity to perform effective high-pressure CO$_2$/CH$_4$ separation and high-productivity methane purification. The effects of the temperature on the structural flexibility and gas separation were systematically investigated by combining XRD analyses, gas adsorption, computer simulation, and dynamic breakthrough experiments. Among these ZIFs, ZIF-78-ht1, with its midlevel locking, exhibited the best CO$_2$/CH$_4$ separation performance, owing to its suitable pore size and structural rigidity during gas adsorption. The findings highlight the importance of deliberate control over a given ZIF's framework dynamics via linker—linker interactions and precise regulation of the inherent flexibility through activation-induced sequential structural locking under different temperatures to improve gas separation under relevant operating conditions. The strategy employed in this work highlights the delicate balance between the porosity and framework rigidity when designing next-generation porous adsorbents.

■ ASSOCIATED CONTENT

ⓢ Supporting Information

The Supporting Information is available free of charge at https://pubs.acs.org/doi/10.1021/jacs.4c00045.

The synthetic procedure, PXRD patterns, NMR and FTIR spectra, SEM pictures, TGA curves, SCXRD results, DSC curves, gas sorption isotherms, and dynamic gas adsorption breakthrough curves (PDF).

Accession Codes

CCDC 2299695−2299698 contains the supplementary crystallographic data for this paper. These data can be obtained free of charge via www.ccdc.cam.ac.uk/data_-request/cif or by emailing data_request@ccdc.cam.ac.uk or by contacting The Cambridge Crystallographic Data Centre, 12 Union Road, Cambridge CB2 1EZ, UK; fax: +44 1223 336033.

■ AUTHOR INFORMATION

Corresponding Author

Yue-Biao Zhang — *School of Physical Science and Technology, Shanghai Key Laboratory of High-Resolution Electron Microscopy, State Key Laboratory of Advanced Medical Materials and Devices, ShanghaiTech University, Shanghai 201210, China;* ⦿ orcid.org/0000-0002-8270-1067; Email: zhangyb@shanghaitech.edu.cn

Authors

Tongtong Xu — *School of Physical Science and Technology, Shanghai Key Laboratory of High-Resolution Electron*

Microscopy, State Key Laboratory of Advanced Medical Materials and Devices, ShanghaiTech University, Shanghai 201210, China; ⓞ orcid.org/0000-0002-0776-5749

Wentao Jiang − *School of Physical Science and Technology, Shanghai Key Laboratory of High-Resolution Electron Microscopy, State Key Laboratory of Advanced Medical Materials and Devices, ShanghaiTech University, Shanghai 201210, China;* ⓞ orcid.org/0000-0002-5376-3381

Yu Tao − *School of Physical Science and Technology, Shanghai Key Laboratory of High-Resolution Electron Microscopy, State Key Laboratory of Advanced Medical Materials and Devices, ShanghaiTech University, Shanghai 201210, China*

Mahmoud Abdellatief − *Synchrotron-light for Experimental Science and Applications in the Middle East (SESAME), Allan 19252, Jordan*

Kyle E. Cordova − *Integrated Materials Systems (iMS) Research Unit, Advanced Research Center, Royal Scientific Society, Amman 11941, Jordan;* ⓞ orcid.org/0000-0002-4988-0497

Complete contact information is available at:
https://pubs.acs.org/10.1021/jacs.4c00045

Notes
The authors declare no competing financial interest.

■ REFERENCES

(1) Phan, A.; Doonan, C. J.; Uribe-Romo, F. J.; Knobler, C. B.; O'Keeffe, M.; Yaghi, O. M. Synthesis, Structure, and Carbon Dioxide Capture Properties of Zeolitic Imidazolate Frameworks. *Acc. Chem. Res.* **2010**, *43*, 58−67.

(2) Zhang, J.-P.; Zhang, Y.-B.; Lin, J.-B.; Chen, X.-M. Metal Azolate Frameworks: From Crystal Engineering to Functional Materials. *Chem. Rev.* **2012**, *112*, 1001−1033.

(3) Eddaoudi, M.; Sava, D. F.; Eubank, J. F.; Adil, K.; Guillerm, V. Zeolite-like metal−organic frameworks (ZMOFs): design, synthesis, and properties. *Chem. Soc. Rev.* **2015**, *44*, 228−249.

(4) Noh, K.; Lee, J.; Kim, J. Compositions and Structures of Zeolitic Imidazolate Frameworks. *Isr. J. Chem.* **2018**, *58*, 1075−1088.

(5) Tan, Y.-X.; Wang, F.; Zhang, J. Design and synthesis of multifunctional metal−organic zeolites. *Chem. Soc. Rev.* **2018**, *47*, 2130−2144.

(6) Wang, H.; Pei, X.; Kalmutzki, M. J.; Yang, J.; Yaghi, O. M. Large Cages of Zeolitic Imidazolate Frameworks. *Acc. Chem. Res.* **2022**, *55*, 707−721.

(7) Tian, Y.-Q.; Cai, C.-X.; Ji, Y.; You, X.-Z.; Peng, S.-M.; Lee, G.-H. $[Co_5(im)_{10} \cdot 2 \ MB]_\infty$: A Metal-Organic Open-Framework with Zeolite-Like Topology. *Angew. Chem., Int. Ed.* **2002**, *41*, 1384−1386.

(8) Huang, X.-C.; Zhang, J.; Chen, X.-M. $[Zn(bim)_2] \cdot (H_2O)_{1.67}$: A metal-organic open-framework with sodalite topology. *Chin. Sci. Bull.* **2003**, *48*, 1531−1534.

(9) Huang, X. C.; Lin, Y. Y.; Zhang, J. P.; Chen, X. M. Ligand-directed strategy for zeolite-type metal-organic frameworks: zinc(II) imidazolates with unusual zeolitic topologies. *Angew. Chem., Int. Ed.* **2006**, *45*, 1557−1559.

(10) Park, K. S.; Ni, Z.; Côté, A. P.; Choi, J. Y.; Huang, R.; Uribe-Romo, F. J.; Chae, H. K.; O'Keeffe, M.; Yaghi, O. M. Exceptional chemical and thermal stability of zeolitic imidazolate frameworks. *Proc. Natl. Acad. Sci. U.S.A.* **2006**, *103*, 10186−10191.

(11) Liu, Y.; Kravtsov, V. C.; Larsen, R.; Eddaoudi, M. Molecular building blocks approach to the assembly of zeolite-like metal−organic frameworks (ZMOFs) with extra-large cavities. *Chem. Commun.* **2006**, 1488−1490.

(12) Wu, T.; Bu, X.; Zhang, J.; Feng, P. New Zeolitic Imidazolate Frameworks: From Unprecedented Assembly of Cubic Clusters to Ordered Cooperative Organization of Complementary Ligands. *Chem. Mater.* **2008**, *20*, 7377−7382.

(13) Zhang, J.; Wu, T.; Zhou, C.; Chen, S.; Feng, P.; Bu, X. Zeolitic Boron Imidazolate Frameworks. *Angew. Chem., Int. Ed.* **2009**, *48*, 2542−2545.

(14) Shi, Q.; Xu, W.-J.; Huang, R.-K.; Zhang, W.-X.; Li, Y.; Wang, P.; Shi, F.-N.; Li, L.; Li, J.; Dong, J. Zeolite CAN and AFI-Type Zeolitic Imidazolate Frameworks with Large 12-Membered Ring Pore Openings Synthesized Using Bulky Amides as Structure-Directing Agents. *J. Am. Chem. Soc.* **2016**, *138*, 16232−16235.

(15) Yang, J.; Zhang, Y.-B.; Liu, Q.; Trickett, C. A.; Gutierrez-Puebla, E.; Monge, M. Á.; Cong, H.; Aldossary, A.; Deng, H.; Yaghi, O. M. Principles of Designing Extra-Large Pore Openings and Cages in Zeolitic Imidazolate Frameworks. *J. Am. Chem. Soc.* **2017**, *139*, 6448−6455.

(16) Zha, X.; Li, X.; Al-Omari, A. A.; Liu, S.; Liang, C.-C.; Al-Ghourani, Aa.; Abdellatief, M.; Yang, J.; Nguyen, H. L.; Al-Maythalony, B.; et al. Zeolite NPO-Type Azolate Frameworks. *Angew. Chem., Int. Ed.* **2022**, *61*, No. e202207467.

(17) Wang, B.; Côté, A. P.; Furukawa, H.; O'Keeffe, M.; Yaghi, O. M. Colossal cages in zeolitic imidazolate frameworks as selective carbon dioxide reservoirs. *Nature* **2008**, *453*, 207−211.

(18) Banerjee, R.; Phan, A.; Wang, B.; Knobler, C.; Furukawa, H.; O'Keeffe, M.; Yaghi, O. M. High-Throughput Synthesis of Zeolitic Imidazolate Frameworks and Application to CO_2 Capture. *Science* **2008**, *319*, 939−943.

(19) Banerjee, R.; Furukawa, H.; Britt, D.; Knobler, C.; O'Keeffe, M.; Yaghi, O. M. Control of Pore Size and Functionality in Isoreticular Zeolitic Imidazolate Frameworks and their Carbon Dioxide Selective Capture Properties. *J. Am. Chem. Soc.* **2009**, *131*, 3875−3877.

(20) Nguyen, N. T. T.; Furukawa, H.; Gándara, F.; Nguyen, H. T.; Cordova, K. E.; Yaghi, O. M. Selective Capture of Carbon Dioxide under Humid Conditions by Hydrophobic Chabazite-Type Zeolitic

Imidazolate Frameworks. *Angew. Chem., Int. Ed.* **2014**, *53*, 10645−10648.

(21) Peng, Y.; Li, Y.; Ban, Y.; Jin, H.; Jiao, W.; Liu, X.; Yang, W. Metal-organic framework nanosheets as building blocks for molecular sieving membranes. *Science* **2014**, *346*, 1356−1359.

(22) Xiang, L.; Sheng, L.; Wang, C.; Zhang, L.; Pan, Y.; Li, Y. Amino-Functionalized ZIF-7 Nanocrystals: Improved Intrinsic Separation Ability and Interfacial Compatibility in Mixed-Matrix Membranes for CO_2/CH_4 Separation. *Adv. Mater.* **2017**, *29*, No. 1606999.

(23) Gong, X.; Wang, Y.; Kuang, T. ZIF-8 based membranes for carbon dioxide capture/separation. *ACS Sustainable Chem. Eng.* **2017**, *5*, 11204−11214.

(24) Ma, X.; Kumar, P.; Mittal, N.; Khlyustova, A.; Daoutidis, P.; Mkhoyan, K. A.; Tsapatsis, M. Zeolitic imidazolate framework membranes made by ligand-induced permselectivity. *Science* **2018**, *361*, 1008−1011.

(25) Gao, Y.; Qiao, Z.; Zhao, S.; Wang, Z.; Wang, J. In situ synthesis of polymer grafted ZIFs and application in mixed matrix membrane for CO2 separation. *J. Mater. Chem. A* **2018**, *6*, 3151−3161.

(26) Hou, Q.; Wu, Y.; Zhou, S.; Wei, Y.; Caro, J.; Wang, H. Ultra-Tuning of the Aperture Size in Stiffened ZIF-8_Cm Frameworks with Mixed-Linker Strategy for Enhanced CO_2/CH_4 Separation. *Angew. Chem., Int. Ed.* **2019**, *58*, 327−331.

(27) Lyndon, R.; You, W.; Ma, Y.; Bacsa, J.; Gong, Y.; Stangland, E. E.; Walton, K. S.; Sholl, D. S.; Lively, R. P. Tuning the Structures of Metal−Organic Frameworks via a Mixed-Linker Strategy for Ethyl-ene/Ethane Kinetic Separation. *Chem. Mater.* **2020**, *32*, 3715−3722.

(28) Aguado, S.; Bergeret, G.; Titus, M. P.; Moizan, V.; Nieto-Draghi, C.; Bats, N.; Farrusseng, D. Guest-induced gate-opening of a zeolite imidazolate framework. *New J. Chem.* **2011**, *35*, 546−550.

(29) Fairen-Jimenez, D.; Moggach, S. A.; Wharmby, M. T.; Wright, P. A.; Parsons, S.; Duren, T. Opening the gate: framework flexibility in ZIF-8 explored by experiments and simulations. *J. Am. Chem. Soc.* **2011**, *133*, 8900−8902.

(30) Ania, C. O.; Garcia-Perez, E.; Haro, M.; Gutierrez-Sevillano, J. J.; Valdes-Solis, T.; Parra, J. B.; Calero, S. Understanding Gas-Induced Structural Deformation of ZIF-8. *J. Phys. Chem. Lett.* **2012**, *3*, 1159−1164.

(31) Zhao, P.; Lampronti, G. I.; Lloyd, G. O.; Wharmby, M. T.; Facq, S.; Cheetham, A. K.; Redfern, S. A. Phase Transitions in Zeolitic Imidazolate Framework 7: The Importance of Framework Flexibility and Guest-Induced Instability. *Chem. Mater.* **2014**, *26*, 1767−1769.

(32) Hobday, C. L.; Woodall, C. H.; Lennox, M. J.; Frost, M.; Kamenev, K.; Duren, T.; Morrison, C. A.; Moggach, S. A. Understanding the adsorption process in ZIF-8 using high pressure crystallography and computational modelling. *Nat. Commun.* **2018**, *9*, No. 1429.

(33) Zhao, P.; Fang, H.; Mukhopadhyay, S.; Li, A.; Rudic, S.; McPherson, I. J.; Tang, C. C.; Fairen-Jimenez, D.; Tsang, S. C. E.; Redfern, S. A. T. Structural dynamics of a metal-organic framework induced by CO_2 migration in its non-uniform porous structure. *Nat. Commun.* **2019**, *10*, No. 999.

(34) Iacomi, P.; Maurin, G. ResponZIF Structures: Zeolitic Imidazolate Frameworks as Stimuli-Responsive Materials. *ACS Appl. Mater. Interfaces.* **2021**, *13*, 50602−50642.

(35) Gao, M.; Huang, R.-K.; Zheng, B.; Wang, P.; Shi, Q.; Zhang, W.-X.; Dong, J. Large breathing effect in ZIF-65(Zn) with expansion and contraction of the SOD cage. *Nat. Commun.* **2022**, *13*, No. 4569.

(36) Zhang, L.; Wu, G.; Jiang, J. Adsorption and Diffusion of CO_2 and CH_4 in Zeolitic Imidazolate Framework-8: Effect of Structural Flexibility. *J. Phys. Chem. C* **2014**, *118*, 8788−8794.

(37) Du, Y.; Mao, K.; Wooler, B.; Sharma, A. K.; Colmyer, D.; Nines, M.; Weston, S. C. Insights into the Flexibility of ZIF-7 and Its Structural Impact in Alcohol Adsorption. *J. Phys. Chem. C* **2017**, *121*, 28090−28095.

(38) Knebel, A.; Geppert, B.; Volgmann, K.; Kolokolov, D. I.; Stepanov, A. G.; Twiefel, J.; Heitjans, P.; Volkmer, D.; Caro, J.

Defibrillation of soft porous metal-organic frameworks with electric fields. *Science* **2017**, *358*, 347−351.

(39) Zhou, S.; Wei, Y.; Li, L.; Duan, Y.; Hou, Q.; Zhang, L.; Ding, L.-X.; Xue, J.; Wang, H.; Caro, J. Paralyzed membrane: Current-driven synthesis of a metal-organic framework with sharpened propene/propane separation. *Sci. Adv.* **2018**, *4*, No. eaau1393.

(40) Hou, Q.; Zhou, S.; Wei, Y.; Caro, J.; Wang, H. Balancing the Grain Boundary Structure and the Framework Flexibility through Bimetallic Metal−Organic Framework (MOF) Membranes for Gas Separation. *J. Am. Chem. Soc.* **2020**, *142* (21), 9582−9586.

(41) Abdul Hamid, M. R.; Qian, Y.; Wei, R.; Li, Z.; Pan, Y.; Lai, Z.; Jeong, H.-K. Polycrystalline metal-organic framework (MOF) membranes for molecular separations: Engineering prospects and challenges. *J. Membr. Sci.* **2021**, *640*, No. 119802.

(42) Gu, Y.; Hua, J.; Chen, J.; Zhu, W.; Hou, R.; Wang, C.; Pan, Y. Rigid-interface-locking of ZIF-8 membranes to enable for superior high-pressure propylene/propane separation. *J. Membr. Sci.* **2023**, *668*, No. 121193.

(43) Xu, T.; Zhou, B.; Tao, Y.; Shi, Z.; Jiang, W.; Abdellatief, M.; Cordova, K. E.; Zhang, Y.-B. Functionality-Induced Locking of Zeolitic Imidazolate Frameworks. *Chem. Mater.* **2023**, *35*, 490−498.

(44) Cho, H. S.; Yang, J.; Gong, X.; Zhang, Y. B.; Momma, K.; Weckhuysen, B. M.; Deng, H.; Kang, J. K.; Yaghi, O. M.; Terasaki, O. Isotherms of Individual Pores by Gas Adsorption Crystallography. *Nat. Chem.* **2019**, *11*, 562−570.

(45) Sarkisov, L.; Martin, R. L.; Haranczyk, M.; Smit, B. On the Flexibility of Metal−Organic Frameworks. *J. Am. Chem. Soc.* **2014**, *136*, 2228−2231.

(46) Lu, T.; Chen, F. Multiwfn: A multifunctional wavefunction analyzer. *J. Comput. Chem.* **2012**, *33*, 580−592.

(47) Zhang, J.; Lu, T. Efficient evaluation of electrostatic potential with computerized optimized code. *Phys. Chem. Chem. Phys.* **2021**, *23*, 20323−20328.

(48) Lu, T.; Chen, Q. Independent gradient model based on Hirshfeld partition: A new method for visual study of interactions in chemical systems. *J. Comput. Chem.* **2022**, *43*, 539−555.

(49) Emamian, S.; Lu, T.; Kruse, H.; Emamian, H. Exploring Nature and Predicting Strength of Hydrogen Bonds: A Correlation Analysis Between Atoms-in-Molecules Descriptors, Binding Energies, and Energy Components of Symmetry-Adapted Perturbation Theory. *J. Comput. Chem.* **2019**, *40*, 2868−2881.

(50) Dubbeldam, D.; Calero, S.; Ellis, D. E.; Snurr, R. Q. RASPA: molecular simulation software for adsorption and diffusion in flexible nanoporous materials. *Mol. Simul.* **2016**, *42*, 81−101.

(51) Manz, T. A.; Limas, N. G. Introducing DDEC6 atomic population analysis: part 1. Charge partitioning theory and method-ology. *RSC Adv.* **2016**, *6*, 47771−47801.

(52) Rappe, A. K.; Casewit, C. J.; Colwell, K. S.; Goddard, W. A., III.; Skiff, W. M. UFF, a full periodic table force field for molecular mechanics and molecular dynamics simulations. *J. Am. Chem. Soc.* **1992**, *114*, 10024−10035.

(53) Mayo, S. L.; Olafson, B. D.; Goddard, W. A. DREIDING: a generic force field for molecular simulations. *J. Phys. Chem. A* **1990**, *94*, 8897−8909.

(54) Gutmann, V. *The Donor-Acceptor Approach to Molecular Interactions*; Plenum: New York, 1978; pp 1−16.

(55) Sutor, D. J. The C−H⋯O Hydrogen Bond in Crystals. *Nature* **1962**, *195*, 68−69.

(56) Desiraju, G. R. The C−H⋯O Hydrogen Bond: Structural Implications and Supramolecular Design. *Acc. Chem. Res.* **1996**, *29*, 441−449.

(57) Yu, H.; Wang, X.; Xu, C.; Chen, D.-L.; Zhu, W.; Krishna, R. Utilizing transient breakthroughs for evaluating the potential of Kureha carbon for CO_2 capture. *Chem. Eng. J.* **2015**, *269*, 135−147.

(58) Zhao, J.; Xie, K.; Singh, R.; Xiao, G.; Gu, Q.; Zhao, Q.; Li, G.; Xiao, P.; Webley, P. A. $Li^+/ZSM-25$ Zeolite as a CO_2 Capture Adsorbent with High Selectivity and Improved Adsorption Kinetics, Showing CO_2-Induced Framework Expansion. *J. Phys. Chem. C* **2018**, *122*, 18933−18941.

I

(59) Lawson, S.; Al-Naddaf, Q.; Newport, K.; Rownaghi, A.; Rezaei, F. Assessment of CO_2/CH_4 Separation Performance of 3D-Printed Carbon Monoliths in Pressure Swing Adsorption. *Ind. Eng. Chem. Res.* **2021**, *60*, 16445−16456.

(60) Lei, J.; Yuan, W.; Shang, J.; Xu, J.; Zhang, P.; Wang, Y.; Li, Y. P.; Zhai, Q. G. Development of a Mixed Multinuclear Cluster Strategy in Metal-Organic Frameworks for Methane Purification and Storage. *Inorg. Chem.* **2023**, *62*, 15195−15205.

(61) Day, M. C.; Selbin, J. *Theoretical Inorganic Chemistry*; Reinhold Publishing Corp.: New York, 1962; pp 285−325.

(62) O'Brien, M. C. M.; Chancey, C. C. The Jahn−Teller effect: An introduction and current review. *Am. J. Phys.* **1993**, *61*, 688−697.

(63) Legendre, C. M.; Damgaard-Møller, E.; Overgaard, J.; Stalke, D. The Quest for Optimal 3 d Orbital Splitting in Tetrahedral Cobalt Single-Molecule Magnets Featuring Colossal Anisotropy and Hysteresis. *Eur. J. Inorg. Chem.* **2021**, *2021*, 3108−3114.

(64) Haszeldine, R. S. Carbon capture and storage: how green can black be? *Science* **2009**, *325*, 1647−1652.

(65) Nugent, P.; Belmabkhout, Y.; Burd, S. D.; Cairns, A. J.; Luebke, R.; Forrest, K.; Pham, T.; Ma, S.; Space, B.; Wojtas, L.; et al. Porous materials with optimal adsorption thermodynamics and kinetics for CO_2 separation. *Nature* **2013**, *495*, 80−84.

(66) Vitillo, J. G.; Smit, B.; Gagliardi, L.; et al. Introduction: Carbon Capture and Separation. *Chem. Rev.* **2017**, *117*, 9521−9523.